Extreme Mechanics Letters 38 (2020) 100758

Contents lists available at ScienceDirect

Extreme Mechanics Letters

journal homepage: www.elsevier.com/locate/eml

Elastically-supported lattices for tunable mechanical topological insulators

Hasan Al Ba'ba'a, Kunhao Yu, Qiming Wang *

Sonny Astani Department of Civil and Environmental Engineering, University of Southern California, Los Angeles, CA 90089, USA

ARTICLE INFO

Article history:
Received 7 April 2020
Received in revised form 30 April 2020
Accepted 30 April 2020
Available online 19 May 2020

Keywords:
Topological insulators
Hexagonal lattices
Quantum Valley Hall Effect
Valley Chern number
Inversion symmetry

ABSTRACT

Emerging mechanical topological insulators based on Quantum Valley Hall Effect (QVHE) offer a myriad of unconventional and robust properties in controlling wave motion. Designing mechanical topological insulators requires a careful assignment of the system's mechanical properties in a specific manner. Consequently, modulating the topological property of a fabricated system is typically challenging. Here, we introduce an externally adding-on mechanism that enables high tunability of QVHE without the need to alter the main fabricated structure. Specifically, we exploit a periodic elastic foundation to control the topological property of a hexagonal lattice. Non-equal stiffnesses of the elastic foundation break the inversion symmetry of the hexagonal lattice, thus introducing the QVHE to the system. A mathematical framework is established to understand the fundamental mechanism and design the topologically protected waveguides by tuning the elastic foundation. The achieved topological insulators exhibit high tolerance over defects. The paradigm in this work opens promising avenues for mechanical metamaterials with tunable topological properties.

1. Introduction

Periodic lattices have facilitated the design of a variety of mechanical and acoustic systems, offering a plethora of exotic physical phenomena not available in nature [1–3]. One of the hallmark features of periodic lattices is their unique interaction with wave propagation, whether in elastic [4] or acoustic [5] media. Having a spatially periodic unit cell constituting lattice structures gives rise to a range of interesting behaviors, such as wave attenuation [6], beaming [7], negative refractive index [8], and cloaking [9]. Engineered lattice materials have imprinted a profound impact on various vibration control and wave propagation aspects, such as wave directivity [10] and steering [11], wave focusing via elastic lenses [12,13], and one-way wave transmission [14,15]. A new frontier in studying wave propagation in periodic lattices is the notion of topological insulators, which has recently witnessed a spurt of research activity in the domain of mechanical systems [16–18]. The growing interest in mechanical topological insulators, initially inspired by their electronic counterpart, stems largely from their robustness and promised immunity against defects and imperfections, among other unusual properties [19]. Of specific interest in this effort is the concept of the *Quantum Valley Hall effect* (QVHE), which manifests itself in hexagonal lattices [20–25]. Topological protection accompanying QVHE emerges when the inversion symmetry of the unit cell is broken while maintaining a third order rotational symmetry C_3. Known for exhibiting degenerate Dirac cones at the Brillouin zone's high-symmetry points, hexagonal lattices with violated inversion symmetry lose the degeneracy at the Dirac cones, and a frequency bandgap opens as a result [18]. Typically, the quantification of topological protection in dynamical systems is accomplished by a metric, referred to as a *topological invariant,* and, in the context of QVHE, the Valley Chern Number (computed at the vicinity of the Dirac cones) is customarily exploited [24,25]. Besides hexagonal lattices, various topologically protected systems with different mechanical and geometrical configurations have been theoretically and experimentally demonstrated. This includes, but is not limited to, coupled pendula [26], bilayered rotational Lieb lattices [27], spatiotemporally modulated lattices [28], quasi-periodic systems [29,30], and gyroscopic systems [31–33].

The design of topological elastic systems requires a careful assignment of the system's mechanical properties in a specific manner. As a result, fabricated structures, often designed to meet a specific requirement, may not allow for modification and adjustments to their topological properties in a later stage, and, thus, impose some practical challenges. This challenge naturally yields to the following question: Is it possible to conceive an externally adding-on mechanism capable of tuning topological properties without alterations to the original system? Motivated by this question, we exploit the idea of periodic elastic foundation as a means to tune, induce, or even nullify QVHE in hexagonal

* Corresponding author.
E-mail address: qimingw@usc.edu (Q. Wang).

https://doi.org/10.1016/j.eml.2020.100758
2352-4316/

structures with existing periodic modulation. The concept of elastic foundation is known to control wave dispersion characteristics in phononic materials [34]; hence, the rationale is utilized here to enable tunability and manifestation of QVHE in hexagonal lattices, a design scheme that remains unexplored in such elastic systems. We focus on a diatomic hexagonal lattice with unequal elastic supports to found a deeper fundamental understanding and, in the process, derive generalized analytical formulations, specifically the unit-cell's Hamiltonian. The latter is of utmost importance to elucidate the physical mechanism of QVHE in elastically supported hexagonal lattices. Unequal masses of the unit cell are considered to demonstrate the tunability of hexagonal structure with existing modulation. We validate the feasibility of using a combination of periodic mass and/or an elastic foundation to tune/induce topologically protected interface modes via the analysis of a supercell with an interface defining the limit of two topologically distinct lattices. The analyses based on the unit cell Hamiltonian and supercell dynamics are further verified by full-scale numerical simulations using a honeycomb finite structure with various configurations of waveguides. We finally show that two entirely different modulation types can co-exist in the same structure while maintaining an operational topological waveguide.

2. Wave dispersion in hexagonal lattices on elastic foundation

2.1. Structural design

We consider a hexagonal lattice constructed from a network of masses, m_1 and m_2, periodically coupled via taut strings with a linear density of ρ, a constant tension T, and an equivalent spring constant of $k = T/a$, where a is the length of the string segment (Fig. 1AC). The coupling strings are rendered massless as large lumped masses $m_{1,2} \gg \rho a$ are assumed. The masses, m_1 and m_2, are supported by a periodic elastic foundation, represented by two types of springs k_1 and k_2, respectively. The elastic foundation is also assumed to be massless, allowing for approximating the system into a lumped parameter model. By virtue of the periodicity, a self-repeating unit cell definition can be conceived as two masses with its elastic connections repeating in two directions, represented by the indices i and j (Fig. 1B).

2.2. Unit cell analysis

2.2.1. Mathematical formulation

Consider the discrete model of the unit cell in Fig. 1C, where the motion of the unit-cell's first and second masses, $u_{i,j}$ and $v_{i,j}$ respectively, is only in the out-of-plane direction (z-direction). The resisting forces from each individual string is a function of its equivalent stiffness and the relative displacement of the two masses on its edges. For instance, the string segment connecting $u_{i,j}$ and $v_{i,j}$ exerts an out-of-plane force of $f_z = T\sin\alpha \approx T\tan\alpha$, which is valid for infinitesimal displacements (See the inset in Fig. 1C). From the geometrical properties, it immediately follows that $\tan\alpha = \Delta/a = (v_{i,j} - u_{i,j})/a$, resulting in $f_z = k(v_{i,j} - u_{i,j})$. Following a similar procedure for the remaining coupling strings, one can show that the complete equations of motion of the unit cell are given by:

$$m_1\ddot{u}_{i,j} + (k_1 + 3k)\,u_{i,j} - k\left(v_{i-1,j} + v_{i,j-1} + v_{i,j}\right) = 0 \tag{1}$$

$$m_2\ddot{v}_{i,j} + (k_2 + 3k)\,v_{i,j} - k\left(u_{i+1,j} + u_{i,j+1} + u_{i,j}\right) = 0 \tag{2}$$

Owing to the structural periodicity, the Bloch theorem can be applied to express Eqs. (1) and (2) solely in terms of the degrees of freedom of the (i, j) unit, i.e. $u_{i,j}$ and $v_{i,j}$ (See [21,35,36] for different examples and detailed discussions). To this end, we define a displacement vector $\mathbf{z}_{i,j} = \left\{u_{i,j} \quad v_{i,j}\right\}^{\mathrm{T}}$ for the cell (i, j), and write $\mathbf{z}_{i\pm1,j\pm1} = \mathrm{e}^{\mathbf{i}(\pm q_1 \pm q_2)}\mathbf{z}_{i,j}$ for its neighboring cells, where $\mathbf{i} = \sqrt{-1}$ is the imaginary unit and the nondimensional wavenumbers q_1 and q_2 are defined as functions of the nondimensional wavenumbers in the x- and y-directions, q_x and q_y respectively,

$$q_1 = \frac{1}{2}\left(\sqrt{3}q_x + q_y\right) \tag{3}$$

$$q_2 = \frac{1}{2}\left(\sqrt{3}q_x - q_y\right) \tag{4}$$

Thus, the governing equations (1) and (2) are condensed in matrix notation:

$$\mathbf{M_c}\ddot{\mathbf{z}}_{i,j} + \mathbf{K_c}\,(\boldsymbol{q})\,\mathbf{z}_{i,j} = 0 \tag{5}$$

where $\ddot{[\,]}$ denotes the second derivative in time and:

$$\mathbf{M_c} = \begin{bmatrix} m_1 & 0 \\ 0 & m_2 \end{bmatrix}, \quad \mathbf{K_c}(\boldsymbol{q}) = \begin{bmatrix} k_1 + 3k & -k\varepsilon^* \\ -k\varepsilon & k_2 + 3k \end{bmatrix} \tag{6}$$

are unit-cell's mass and stiffness matrices, respectively. Condensing the degrees of freedoms as in Eq. (5) renders the unit-cell's stiffness matrix $\mathbf{K_c}\,(\boldsymbol{q})$ a function of the dimensionless wavevector $\boldsymbol{q} = \{q_1, q_2\}^{\mathrm{T}}$ with $\varepsilon = (1 + \mathrm{e}^{\mathbf{i}q_1} + \mathrm{e}^{\mathbf{i}q_2})$ and ε^* denotes its complex conjugate. To reduce the number of studied variables, we first introduce mass and stiffness contrasts, μ and γ respectively, for the masses and elastic supports, which are mathematically expressed as:

$$\mu = \frac{m_1 - m_2}{m_1 + m_2} \tag{7}$$

$$\gamma = \frac{k_1 - k_2}{k_1 + k_2} \tag{8}$$

These two parameters are of key importance in the analysis and span the range $\gamma, \mu \in [-1, 1]$. To account for the stiffness ratio of the elastic foundation and main structure, we define a mean value κ of normalized elastic foundation stiffnesses (with respect to the stiffness k):

$$\kappa = \frac{k_1 + k_2}{2k} \tag{9}$$

In analogy, the masses are parameterized as:

$$m = \frac{m_1 + m_2}{2} \tag{10}$$

Making use of Eqs. (7) through (10), we can express the masses as $m_1 = m\,(1 + \mu)$ and $m_2 = m\,(1 - \mu)$, while the stiffnesses are $k_1 = \kappa k\,(1 + \gamma)$ and $k_2 = \kappa k\,(1 - \gamma)$, thus covering the theoretically infinite possible ratios of k_2/k_1 (or m_2/m_1). Note that $\gamma = 0$ ($\mu = 0$) refers to a situation where both k_1 and k_2 (m_1 and m_2) are equal, while the extreme values of $\gamma = \pm1$($\mu = \pm1$) mandates that either of the two parameters is set to zero. Additionally, a negative value of $\gamma(\mu)$ implies that $k_2 > k_1$ ($m_2 > m_1$) and vice versa. Finally, plugging in the introduced parametrization in the equation of motion (5) produces:

$$m\mathcal{M}\ddot{\mathbf{z}}_{i,j} + k\mathcal{K}\,(\boldsymbol{q})\,\mathbf{z}_{i,j} = 0 \tag{11}$$

where

$$\mathcal{M} = \begin{bmatrix} 1 + \mu & 0 \\ 0 & 1 - \mu \end{bmatrix}, \qquad \mathcal{K}\,(\boldsymbol{q}) = \begin{bmatrix} 3 + \kappa(1 + \gamma) & -\varepsilon^* \\ -\varepsilon & 3 + \kappa(1 - \gamma) \end{bmatrix} \tag{12}$$

2.2.2. System's Hamiltonian

To demonstrate the QVHE in the considered hexagonal lattice, we aim to find a mathematical expression of the system's Hamiltonian, typically derived from the eigenvalue problem of

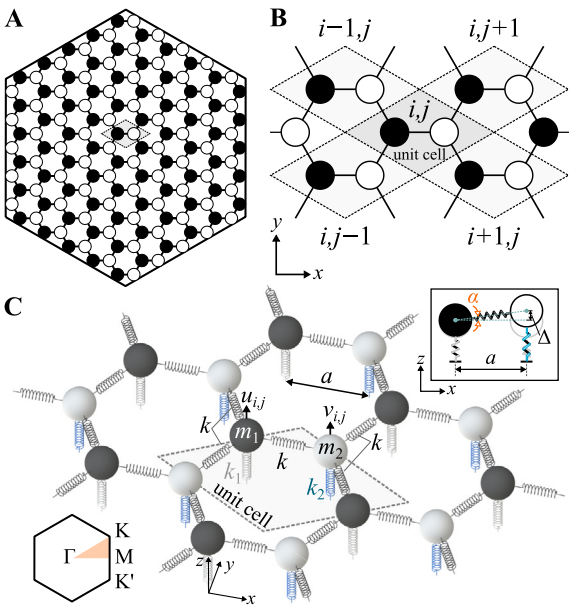

Fig. 1. (A) Schematic of a honeycomb structure constituted from a network of hexagonal unit cells (shown in dashed lines). (B) A close-up of the definition of the unit cell and the respective indexing of the neighboring cells. (C) Three-dimensional schematics of the unit cell and its corresponding inertial and elastic properties. The inset shows an illustrative schematics of the relative displacement of two neighboring cells and the corresponding geometrical parameters. The Irreducible Brillouin Zone (IBZ) is provided for reference.

the mechanical system [27]. Applying a harmonic solution $\ddot{\mathbf{z}}_{i,j} = -\omega^2 \mathbf{z}_{i,j}$ as the first step, with ω being the angular excitation frequency, Eq. (11) can be written as:

$$\frac{k}{m}\begin{bmatrix} 3+\kappa(1+\gamma) & -\varepsilon^* \\ -\varepsilon & 3+\kappa(1-\gamma) \end{bmatrix}\begin{Bmatrix} u_{i,j} \\ v_{i,j} \end{Bmatrix} = \omega^2 \begin{bmatrix} 1+\mu & 0 \\ 0 & 1-\mu \end{bmatrix}\begin{Bmatrix} u_{i,j} \\ v_{i,j} \end{Bmatrix} \tag{13}$$

Following the scheme in Ref. [21], we introduce a new basis $\mathbf{x}_{i,j} = \mathbf{P}\mathbf{z}_{i,j}$, where

$$\mathbf{P} = \begin{bmatrix} \sqrt{1+\mu} & 0 \\ 0 & \sqrt{1-\mu} \end{bmatrix} \tag{14}$$

to reduce Eq. (13) to

$$\frac{k}{m}\mathbf{H}\mathbf{x}_{i,j} = \omega^2 \mathbf{x}_{i,j} \tag{15}$$

Such that $\mathbf{H} = \mathbf{P}^{-1}\mathcal{K}\mathbf{P}^{-1}$ is the Hamiltonian and its explicit form reads:

$$\mathbf{H} = \begin{bmatrix} \dfrac{3+\kappa\,(1+\gamma)}{(1+\mu)} & -\dfrac{\varepsilon^*}{\sqrt{1-\mu^2}} \\ -\dfrac{\varepsilon}{\sqrt{1-\mu^2}} & \dfrac{3+\kappa\,(1-\gamma)}{(1-\mu)} \end{bmatrix} \tag{16}$$

If the denominator of $\mathbf{H}$ diagonal elements is unified to be $(1-\mu^2)$, a few mathematical manipulations lead to a simpler form of the Hamiltonian:

$$\mathbf{H} = \frac{1}{\sqrt{1-\mu^2}}\mathcal{H} \tag{17}$$

where

$$\mathcal{H} = \begin{bmatrix} \Omega_s^2 + \vartheta & -\varepsilon^* \\ -\varepsilon & \Omega_s^2 - \vartheta \end{bmatrix} \tag{18}$$

and

$$\vartheta = \frac{\kappa\gamma - (3+\kappa)\,\mu}{\sqrt{1-\mu^2}} \tag{19}$$

$$\Omega_s = \sqrt{\frac{3+\kappa(1-\gamma\mu)}{\sqrt{1-\mu^2}}} \tag{20}$$

are denoted here as the *tuning parameter* and *central bandgap frequency*, respectively. Introducing a normalized frequency $\Omega = \frac{\omega}{\omega_0}$, with

$$\omega_0 = \sqrt{\frac{k}{m\sqrt{1-\mu^2}}} \tag{21}$$

completes the derivation of the eigenvalue problem:

$$\mathcal{H}\mathbf{x}_{i,j} = \Omega^2 \mathbf{x}_{i,j} \tag{22}$$

In pursuit of comprehending the lattice's topological properties, we further manipulate the Hamiltonian $\mathcal{H}$ in Eq. (18) in an effort to express it as a summation of Pauli matrices $\boldsymbol{\sigma}_l$:

$$\boldsymbol{\sigma}_l = \begin{bmatrix} \delta_{l,0} + \delta_{l,3} & \delta_{l,1} - \mathbf{i}\delta_{l,2} \\ \delta_{l,1} + \mathbf{i}\delta_{l,2} & \delta_{l,0} - \delta_{l,3} \end{bmatrix} \tag{23}$$

where $l = 0, 1, 2, 3$ and $\delta_{[.]}$ is the Kronecker delta. Note here that the zeroth Pauli matrix $\boldsymbol{\sigma}_0$ is the unit matrix and it is combined with the definition in Eq. (23) for mathematical convenience. The normalized Hamiltonian $\mathcal{H}$ now reads

$$\mathcal{H} = \sum_{l=0,1,2,3} h_l \boldsymbol{\sigma}_l \tag{24}$$

and

$$h_0 = \Omega_s^2 \tag{25}$$

$$h_1 = (1 + \cos(q_1) + \cos(q_2)) \tag{26}$$

$$h_2 = (\sin(q_1) + \sin(q_2)) \tag{27}$$

$$h_3 = \vartheta \tag{28}$$

Each of the terms in Eqs. (25) through (28) symbolizes a contribution to the band structure of the hexagonal lattice and its topological properties. While the first term $h_0 = \Omega_s^2$ only shifts the eigenvalues of the Hamiltonian and does not change the

topology of the band structure, the second and third terms are key for forming Dirac cones. The fourth and last term, i.e. Eq. (28), mathematically signifies the breakage of inversion symmetry for non-zero values of ϑ, as evident from its association with $\boldsymbol{\sigma}_3$. The latter is, in addition, essential for opening a frequency bandgap around the central frequency Ω_s and, as a result, lifts the degeneracy at Dirac cones as will be elaborated in the upcoming section.

2.2.3. Dispersion relation and bandgap width

The dispersion relation can be derived from the eigenvalue problem in Eq. (22) via direct computation of $|\mathcal{H} - \Omega^2\mathbf{I}| = 0$:

$$\left(\Omega^2 - \Omega_s^2\right)^2 - \vartheta^2 - |\varepsilon|^2 = 0 \tag{29}$$

Each of Eq. (29) solutions dictate the dispersion surfaces, namely the acoustical Ω_- and optical Ω_+, surfaces, and their explicit forms (after expanding the term $|\varepsilon|^2$) are expressed as:

$$\Omega_\pm = \sqrt{\Omega_s^2 \pm \sqrt{\vartheta^2 + 1 + 4\cos\left(\frac{q_y}{2}\right)\left[\cos\left(\frac{\sqrt{3}}{2}q_x\right) + \cos\left(\frac{q_y}{2}\right)\right]}} \tag{30}$$

Setting ϑ to zero and shifting the frequencies by Ω_s recovers the typical dispersion surfaces of conventional graphene with six Dirac cones at the corners of the Brillouin zone, given that the inversion symmetry of the lattice is preserved. It is important to emphasize that the dispersion relation is not influenced by the change in the basis introduced in Eq. (14) and an identical result can be obtained by simply deriving the determinant of the dynamic stiffness matrix $\mathbf{D_c} = \mathbf{K_c} - \omega^2\mathbf{M_c}$ and setting it to zero.

For the considered hexagonal lattice, the coordinates of IBZ vertices (shown in the inset of Fig. 1C) are written as: $\Gamma = (0, 0)$, $\mathrm{M} = \left(\frac{2\pi}{\sqrt{3}}, 0\right)$ and $\mathrm{K} = \left(\frac{2\pi}{\sqrt{3}}, \frac{2\pi}{3}\right)$, where the centers of the Dirac cones are located at the K (K′) points. For $\vartheta \neq 0$, Dirac cone degeneracies at the K (K′) points are lifted, and a bandgap opens with lower and upper limits, Ω_l and Ω_u:

$$\Omega_{u,l} = \sqrt{\Omega_s^2 \pm |\vartheta|} \tag{31}$$

which yields a bandgap width

$$\Delta\Omega = \Omega_u - \Omega_l = \sqrt{2\left(\Omega_s^2 - \sqrt{\Omega_s^4 - \vartheta^2}\right)} \tag{32}$$

The grounded springs, in addition, induce a zero-frequency bandgap starting at $\Omega = 0$, as its name implies, and ending at $\Omega_z = \sqrt{\Omega_s^2 - \sqrt{\vartheta^2 + 9}}$, as derived from Ω_- in Eq. (30) at the Γ point. The second solution Ω_+ at the Γ point, on the other hand, defines the cutoff frequency $\Omega_c = \sqrt{\Omega_s^2 + \sqrt{\vartheta^2 + 9}}$ of the discrete lattice and represents the opening frequency of an unbounded stop-band.

All in all, changing the sign of ϑ neither influences the bandgap width $\Delta\Omega$ nor the overall shape of dispersion surfaces, as evident from Eqs. (30) through (32). In addition, one type of modulation in a hexagonal lattice, either a mass-only or a stiffness-only modulation, suffices for opening a frequency bandgap (regardless of the stiffness ratio κ) and guarantees a finite width of the bandgap splitting the dispersion surfaces, i.e. $\Delta\Omega = 0$. In contrast, having two types of modulation simultaneously does not always guarantee bandgap emergence. The latter follows from ϑ expression in Eq. (19) which implies that specific combinations of the parameters μ, γ and κ can yield $\vartheta = 0$, interestingly with the presence of elastic and inertial modulations (i.e. $\mu \neq 0$ and $\gamma \neq 0$). For a given value of κ, it is straightforward to establish that the linear equation

$$\gamma = \frac{3 + \kappa}{\kappa}\mu \tag{33}$$

forces the bandgap to close and, consequently, defines the critical condition for the topological transition.

2.2.4. Berry curvature and Valley Chern number

Dispersion relation analyses presented in Section 2.2.3 represent the eigenvalues describing the dynamics of the unit cell. Next, we turn our attention to the associated eigenvectors of the system dynamics, which dictates the Berry curvature and Valley Chern number [24]. Upon plugging in the analytical eigenvalues of the Hamiltonian, and with a few symbolic manipulations, the eigenvectors are:

$$\mathbf{x}_\pm = \frac{1}{\sqrt{2}}\begin{Bmatrix} \sqrt{\frac{\varepsilon^*}{|\varepsilon|}\left(1 \pm \frac{\vartheta}{|\lambda|}\right)} \\ \mp\sqrt{\frac{\varepsilon}{|\varepsilon|}\left(1 \mp \frac{\vartheta}{|\lambda|}\right)} \end{Bmatrix} \tag{34}$$

such that $\mathbf{x}_\pm^{\mathrm{T}}\mathbf{x}_\pm = 1$ and $|\lambda| = \left|\Omega_\pm^2 - \Omega_s^2\right| = \sqrt{|\varepsilon|^2 + \vartheta^2}$ is a shifted eigenvalue. The derived eigenvectors in Eq. (34) further evince the independence of the band structure topology on the term Ω_s^2 as subsequent derivations of the Berry curvature is primarily based on such eigenvectors. For a discrete lattice with two degrees of freedom, the Berry curvature $\mathcal{F}(\boldsymbol{q})$ is reduced to a single term for each of the dispersion bands, such that [21]

$$\mathcal{F}_\pm(\boldsymbol{q}) = \frac{\mathbf{i}}{\left(\omega_+^2 - \omega_-^2\right)^2}\left[\left[\mathbf{u}_\mp^{\mathrm{T}}\frac{\partial\mathbf{K_c}}{\partial q_x}\mathbf{u}_\pm\mathbf{u}_\pm^{\mathrm{T}}\frac{\partial\mathbf{K_c}}{\partial q_y}\mathbf{u}_\mp\right] - \boldsymbol{c}.\boldsymbol{c}.\right] \tag{35}$$

for an eigenvalue problem of the form $\omega_\pm^2\mathbf{M_c}\mathbf{u}_\pm = \mathbf{K_c}\mathbf{u}_\pm$, with a mass-normalized eigenvector $\mathbf{u}_\pm$, i.e. $\mathbf{u}_\pm^{\mathrm{T}}\mathbf{M_c}\mathbf{u}_\pm = 1$. Note here that c.c. denotes the complex conjugate. Based on the derivations in Section 2.2.2, it is straightforward to establish that Eq. (35) is equivalent to evaluating:

$$\mathcal{F}_\pm(\boldsymbol{q}) = \frac{\mathbf{i}}{4|\lambda|^2}\left[\left[\mathbf{x}_\mp^{\mathrm{T}}\frac{\partial\mathcal{H}}{\partial q_x}\mathbf{x}_\pm\mathbf{x}_\pm^{\mathrm{T}}\frac{\partial\mathcal{H}}{\partial q_y}\mathbf{x}_\mp\right] - \boldsymbol{c}.\boldsymbol{c}.\right] \tag{36}$$

in accordance with the eigenvalue problem in Eq. (22). Performing lengthy, albeit straightforward, symbolic manipulations, the Berry curvature boils down to a concise expression (Details are in Supplementary Material Note 1):

$$\mathcal{F}_\pm(\boldsymbol{q}) = \frac{\mp\sqrt{3}\vartheta\sin\left(q_y\right)}{4\sqrt{\left(\vartheta^2 + |\varepsilon|^2\right)^3}} \tag{37}$$

To obtain the Valley Chern number C_v, we linearize our Hamiltonian in the vicinity of the K (K′) point based on perturbed values of the wavenumbers Δq_x and Δq_y. Following a multivariable Taylor expansion of the Hamiltonian around Dirac cones [37], the first-order correction linear term is:

$$\Delta\mathcal{H} = \vartheta\boldsymbol{\sigma}_3 + \nu(\tau\Delta q_y\boldsymbol{\sigma}_1 - \Delta q_x\boldsymbol{\sigma}_2) \tag{38}$$

where $\nu = \frac{\sqrt{3}}{2}$ and the variable $\tau = \pm 1$ is to distinguish between K and K′ points, respectively. This linearized Hamiltonian $\Delta\mathcal{H}$ has been shown to have an approximated Berry curvature near K and K′ points of the form [38]:

$$\hat{\mathcal{F}}_\pm(\Delta q_x, \Delta q_y) = \mp\frac{\tau\vartheta\nu^2}{2\sqrt{\left(\vartheta^2 + \nu^2\Delta q^2\right)^3}} \tag{39}$$

where $\Delta q = \sqrt{\Delta q_x^2 + \Delta q_y^2}$. Finally, the Valley Chern number C_v is evaluated via the following integral definition

$$C_v = \frac{1}{2\pi} \iint \hat{\mathcal{F}}_{\pm}(\Delta q_x, \Delta q_y) d\Delta q_x d\Delta q_y \tag{40}$$

which, for small values of ϑ, converges to [38]:

$$C_v^{\pm} = \mp \frac{1}{2} \tau \mathbf{sgn}[\vartheta] \tag{41}$$

However, as ϑ increases, C_v is expected to move away from its theoretical value and start losing its quantization as $\mp\frac{1}{2}$, which is a direct consequence of the Berry curvature being not strongly localized [39,40]. Moreover, numerically obtained C_v from complex structural models may also lack such a quantization, understandably due to numerical approximations [24]. Nonetheless, theoretical values of C_v can be regarded as reference values for obtaining the number of localized in-gap modes at an interface merging two topologically distinct configurations. For instance, an interface between two lattices with $\vartheta > 0$ and $\vartheta < 0$ should exhibit a single in-gap mode, which can be calculated via $|C_v(\vartheta > 0) - C_v(\vartheta < 0)| = 1$ [39,40].

2.2.5. Numerical example

Fig. 2 shows a comprehensive numerical example of the unit cell analyses with the mass and stiffness contrast parameters being $\mu = \gamma = \pm 0.5$ and $\kappa = 1$. These combinations of values provide tuning parameters of $\vartheta = \mp\sqrt{3}$. In Fig. 2A(i), the Berry curvature and dispersion diagram, corresponding to the first scenario $\vartheta = -\sqrt{3}$, are depicted, where the Berry curvature for the second mode at point K′ and K, respectively, have negative and positive signs. Meanwhile, the theoretical Valley Chern numbers C_v at the K point for the lower and upper limits of the frequency bandgaps are $-\frac{1}{2}$ and $+\frac{1}{2}$, respectively. As we transition from $\vartheta = -\sqrt{3}$ to its positive counterpart following the line of $\mu = \gamma$ (shown in Fig. 2B), the topological transition occurs at $\mu = \gamma = 0$ where the tuning parameter ϑ is zeroed out and the frequency bandgap closes as a consequence (Fig. 2A(ii)). Passing the threshold at the transition line invokes the Berry curvature to switching signs, simultaneously with C_v, as illustrated in Fig. 2A(iii). The dispersion relations for $\vartheta = \pm\sqrt{3}$ have no apparent difference, although their band topologies are distinct as evident from the sign change in their topological invariant, the Valley Chern number. This is also emphasized by the band inversion phenomenon that occurs alongside the topological transition as seen in Fig. 2C, which cannot be perturbed as long as the bandgap remains open.

Revisiting Fig. 2B, it is clearly observed that an appropriate adjustment to the stiffness contrast γ, while keeping a constant μ, is capable of closing the bandgap when the condition $\gamma = 4\mu$ (for the case of $\kappa = 1$) is met. As a case in point, if we start from $\mu = \gamma = 0.2$ ($\vartheta < 0$), increasing γ until 0.8 closes the bandgap and the tuning parameter ϑ is zeroed out, while it changes ϑ sign when $\gamma > 0.8$ and the bandgap subsequently opens. Such an interesting behavior might be accomplished on demand by incorporating tunable active stiffness elements (e.g. piezoelectric materials [10,41]) in lattice's elastic foundations.

2.3. Dynamics of honeycomb structures with waveguides

2.3.1. Interface analysis

To design a topologically protected waveguide, we first carry out eigenfrequency analysis for an interface created by merging two systems with opposite signs of ϑ (and C_v), to attain a localized mode at such an interface. Hence, we construct a one-dimensional finite chain of coupled masses in a periodic manner, with the periodicity order intentionally flipped at the middle interface. The second spatial direction is emulated by imposing a Bloch wave solution on the orthogonal direction of the chain (Related mathematical formulation is presented in Supplementary Material Note 2). The results of the simulations, with identical parameters used in Fig. 2A, are shown in Fig. 3. Here, two interface types are presented: the first interface type starts with $\vartheta > 0$ whilst the second type starts with $\vartheta < 0$; both of which switch the sign of ϑ midway of the chain. The central observation in Fig. 3 is the emergence of a single interface in-gap mode for both types of interfaces (presented via the orange solid lines), which is vital for designing topological waveguides. Changing ϑ sign, however, shifts the frequency range of such interface modes within the bandgap, which will be further emphasized in the finite system simulations. It is noteworthy that an additional mode (shown in blue line) exists within the stop-band frequencies, i.e. $\Omega > \Omega_c$, only for the first interface type, where the second interface type lacks such a mode.

2.3.2. Examples of robust waveguide

The performed interface analysis in the previous section gives an insight into the design of waveguides, especially their operational frequency ranges. Here, we investigate four types of waveguides in a honeycomb structure with a prescribed finite number of masses, which are graphically depicted in Fig. 4A. For ease of reference, we assign the letters I, V, L, and Z, respectively to these four waveguides, which are inspired from their geometrical shape. All honeycomb structures consist of five masses on each of its sides ($n_s = 5$) and a total number of degrees of freedom of $n_t = 6n_s^2 = 150$ (See Supplementary Material Note 3). Starting with the first interface type, i.e. $\vartheta < 0$ and $\vartheta > 0$, as in Fig. 4B, all waveguides with their diverse geometrical shapes greatly confine the wave propagation along its trajectory with minimal wave penetration around it if excited within a bandgap frequency (shown here for a frequency of $\Omega = 2$). Identical waveguide shapes formed from the second interface type (i.e. reversed signs of ϑ) qualitatively resemble that of the first, albeit with a slightly different operational range of frequencies (For instance, an excitation frequency of $\Omega = 1.8$ as in Fig. 4C).

What dictates the operational frequency range, besides the requirement of being within the bandgap, is the natural frequencies distribution of the dynamical structure under consideration. Systematic eigenfrequency analysis for all honeycomb structures in Fig. 4 is presented in Fig. 5, where the mode number is plotted against the value of its normalized natural frequency. As anticipated, the excitation frequencies in all simulations in Fig. 4B and C lie within the location of natural frequencies pertaining to interface modes, which are shown as orange dots in Fig. 5A and B, respectively. In addition, the bulk modes depicted as black circles in Fig. 5 are in an excellent agreement with the frequency ranges of both dispersion branches and interface analysis (Figs. 2 and 3, respectively). As predicted in the interface analysis in Fig. 3A for the first interface type, the modes emerging in the stop-band region $\Omega > \Omega_c$ are also found in the finite honeycomb structural dynamics, as clearly seen in all cases in Fig. 5A. However, such modes are not always guaranteed and vary based on the system parameters (See Supplementary Material Note 4).

Next, we shall demonstrate the robustness of the designed waveguides in Fig. 4. As an example, we simulate the interface Z depicted in Fig. 4A after intentional alteration in the waveguide's elastic foundation. The provoked defects along the path are created by removing the elastic supports in designated places, shown as red dots in Fig. 6A. Performing the simulation at an identical excitation frequency to that in Fig. 4B, very negligible changes in the waveguide dynamics relative to that in Fig. 4B are observed (whether the defects are small or large in number as seen in Fig. 6B). Additionally, the localization of the mode at the

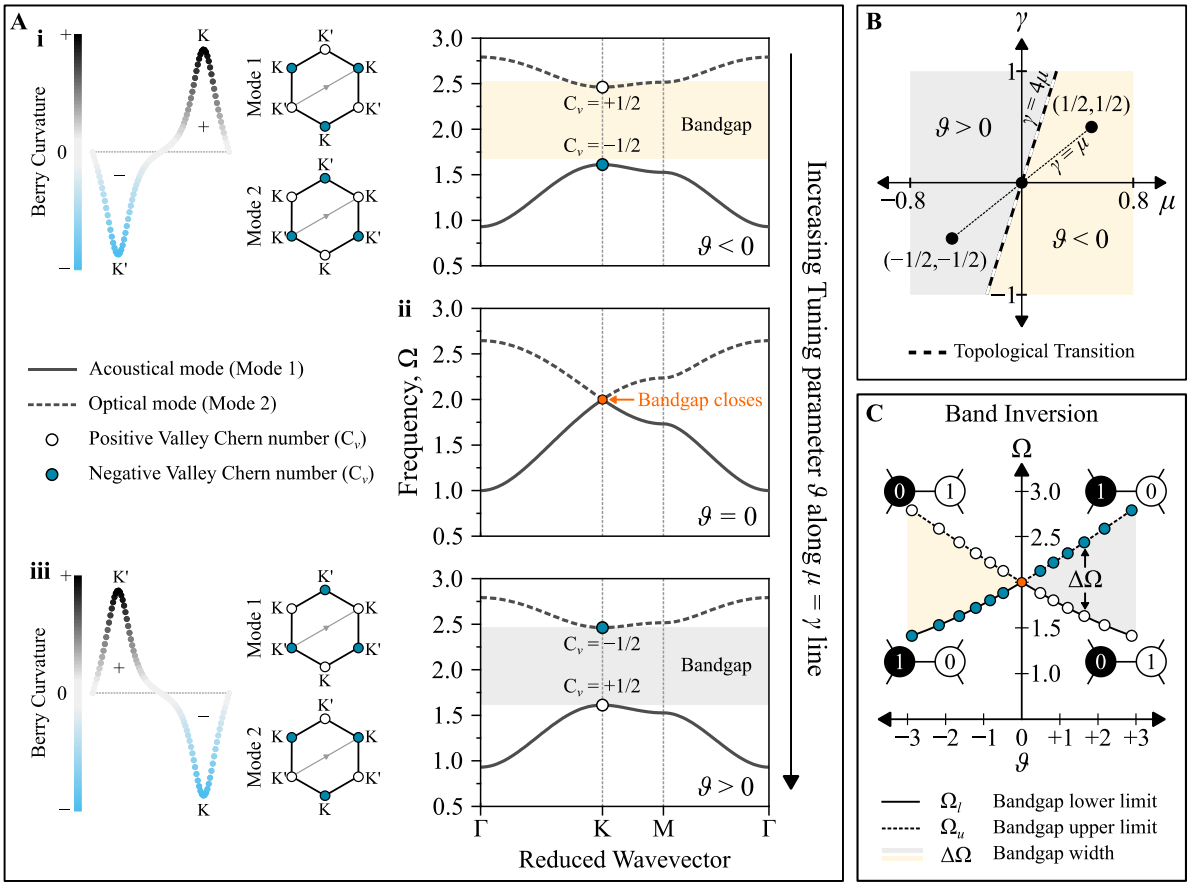

Fig. 2. (A) Representative dispersion diagrams of the unit cell in Fig. 1C with (i) negative, (ii) zero and (iii) positive tuning parameter ϑ. The sign of the valley Chern number C_v changes in association with the Berry curvature, which is also shown in the left panels of subfigures (i) and (iii). (B) The condition of topological transition and the sign of the tuning parameter ϑ over a swept range of mass and stiffness contrasts. (C) The evolution of frequency bandgap limits with varying the tuning parameter ϑ along the line $\gamma = \mu$ shown in subfigure B.

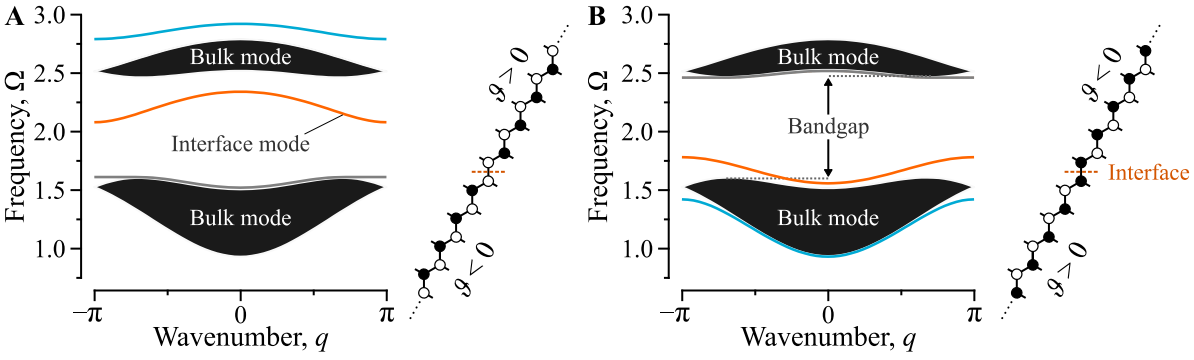

Fig. 3. Eigenfrequency analysis of a supercell comprised of a finite number of masses with the lattice starting with negative (A) and positive (B) ϑ, with an absolute value of $|\vartheta| = \sqrt{3}$. The interface splits the periodic chain in half, where the sign of the tuning parameter flips. The structure is assumed infinite in the orthogonal direction of the extended chain by applying the Bloch wave solution with a non-dimensional wavenumber q. (For interpretation of the references to color in this figure legend, the reader is referred to the web version of this article.)

interface is maintained as originally designed, which is clearly seen from the simulation contours in Fig. 6B. This robustness remains intact as long as the defects are not severe enough to close the bandgap and result in topological transition.

2.3.3. Waveguide design with in-homogenous modulations

The generality of the presented analysis extends beyond the design of waveguide via merging two identical diatomic lattice structures with flipped periodicity order, as demonstrated in the numerical simulations in Section 2.3.2. Based on Eq. (19), the parameter ϑ can be non-zero with negative or positive signs without the need for modulating both masses and stiffnesses (i.e. with either of the mass or stiffness contrasts being zero). The question remains, however, whether two systems with different types of modulations can still allow topological properties to manifest themselves.

Here, we first plot the dispersion diagram for a mass and stiffness modulations with comparable bandgap width and frequency

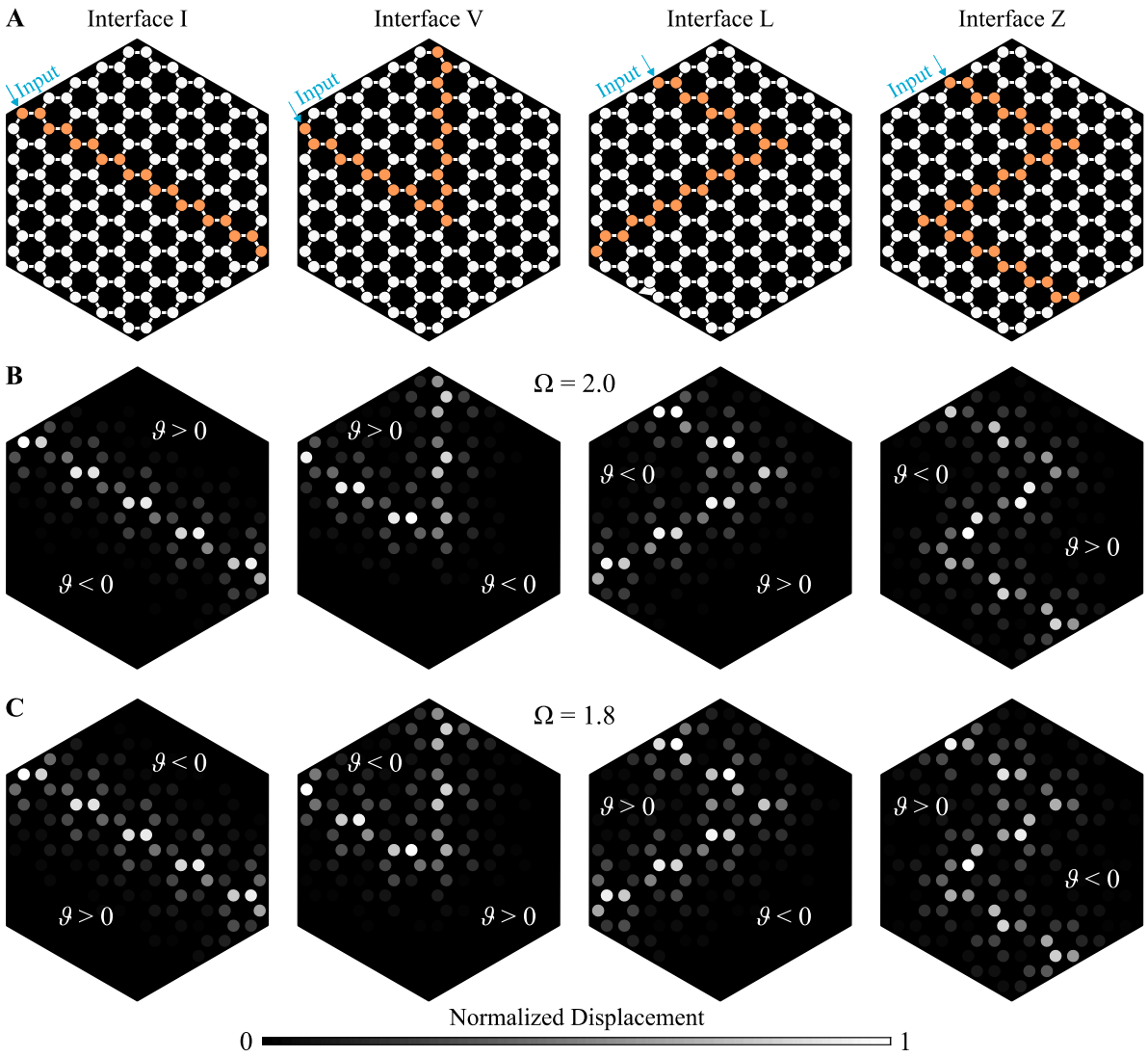

Fig. 4. (A) Schematics of four waveguide designs: I, V, L, and Z, which are highlighted by the orange-colored masses. The sign of the tuning parameter ϑ switches upon passing through the interface. (B, C) Numerical analysis of the honeycomb structure for excitation at one end of the interface as shown in (A). The first set of cases in (B) has $\vartheta < 0$ at the left portion of the structure, while the second set in (C) has $\vartheta > 0$, with excitation frequencies of $\Omega = 2$ and $\Omega = 1.8$, respectively. A black background is added in all schematics for better visualization of the results. (For interpretation of the references to color in this figure legend, the reader is referred to the web version of this article.)

range, and the result is shown in Fig. 7A. The parameters used in these two examples are (i) $\gamma = 0$ and $\mu = 0.25$ for the first case, and (ii) $\mu = 0$ and $\gamma = 1$ for the second case, while the stiffness ratio $\kappa = 1$ remains unchanged as in previous simulations. These choices of parameter combinations result in ϑ being negative and positive, respectively. As expected, the occurrence of band inversion is evident as seen from the eigenmodes in the insets. Performing the interface analysis reveals that in-gap interface mode only appears for the cases of μ and γ having identical signs, corresponding to a change in the sign of the tuning parameter ϑ, while vanishes otherwise (Fig. 7B). Furthermore, we re-simulate the Z-interface presented in Fig. 4 but with the interface now separating two modulation types rather than only re-ordering the masses and springs pattern with exact dispersion diagrams. The results are shown in Fig. 7C and, as expected, are in an excellent agreement with the simulations in Fig. 4 for the case of γ and μ being positive. The topological interface becomes ineffective and does not allow waves to propagate within the bandgap if, for instance, the spring contrast γ changes its sign (i.e. the order of the springs is flipped), as it ultimately results in an identical sign of ϑ throughout the honeycomb structure; this further emphasizes the role of springs foundation in controlling QVHE. Additional analyses pertaining to in-homogenous waveguiding are presented in Supplementary Material Note 5.

3. Conclusions

In summary, we present a generalized theoretical framework of the Quantum Valley Hall Effect (QVHE) in hexagonal lattices supported by a periodic elastic foundation. It has been shown that a periodic modulation of the elastic foundation suffices to break the inversion symmetry of the lattice, which is a requirement for inducing QVHE. Modulations in the lattice's lumped masses, in conjunction with the elastic foundation, has also been shown to be capable of inducing QVHE, providing that an effective tuning parameter ϑ combining both modulation effects has a non-zero value. Interestingly, if the system is modulated by mass only, a proper modulation of the elastic foundation can nullify the QVHE and closes the frequency bandgap consequently. The latter could

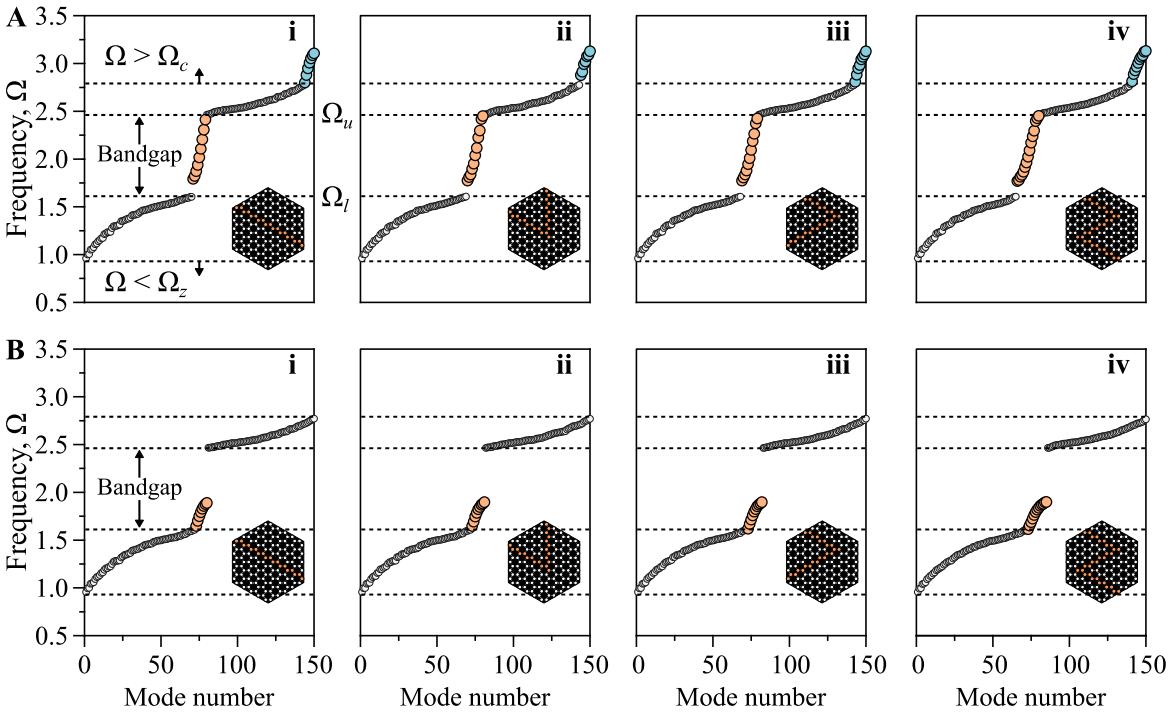

Fig. 5. (A, B) The natural frequencies of the honeycomb structure in Fig. 4B and C, where the subfigures i through iv represent the cases of I, V, L, and Z shaped waveguides, respectively. (For interpretation of the references to color in this figure legend, the reader is referred to the web version of this article.)

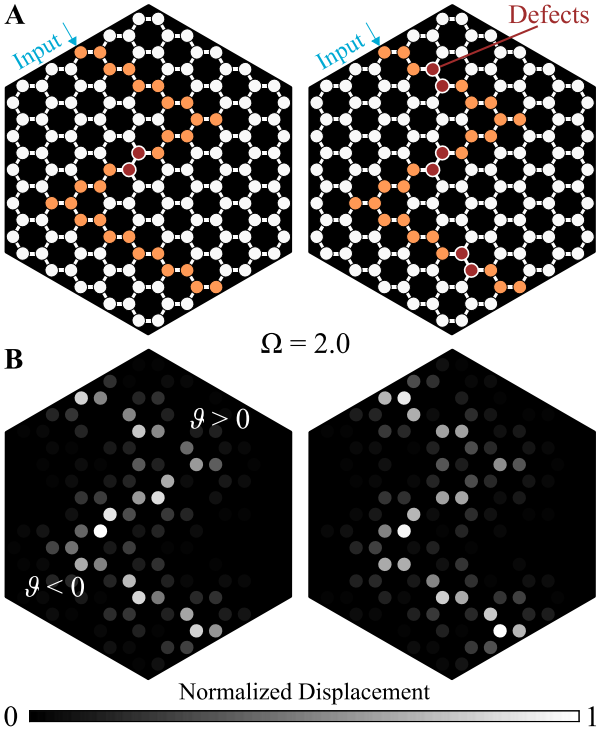

Fig. 6. Robustness test of the Z shaped waveguide: (A) Defects in multiple places are imposed in the structure and compared to the nominal waveguide design without defects (Fig. 4). (B) The frequency response at $\Omega = 2$ of the lattice structure for all cases, showing a negligible difference in their displacement profile. (For interpretation of the references to color in this figure legend, the reader is referred to the web version of this article.)

be of interest from a practical standpoint of view, owing to the fact that actively modulating stiffness has been more successfully and widely achieved in the domain of periodic structures (For instance, piezoelectric materials [42], magnetoactive materials [5], and thermo-responsive material [43]). Furthermore, the proposed design method may be validated experimentally by incorporating such smart materials with on-demand modulation of supporting elastic foundation for potential tunable engineering applications.

Creating a waveguide via merging two topologically distinct lattices guarantees an interface mode at their intersection, which has been emphasized by numerical simulations of several shapes of waveguide trajectories. The robustness of such topologically protected waveguides has been further confirmed by deliberately placing defects along their paths. Given the generality of the proposed analysis, a topologically protected interface can also be created by two different types of modulations (i.e. mass-only and stiffness-only) as along as a different sign of the tuning parameter ϑ is maintained.

The analysis presented in this effort epitomized an alternative design mechanism for QVHE, which relies heavily on the modulation of the supporting elastic foundation. That is, having an elastic foundation mitigates the need for altering the design of the main structure, as such structural modifications are no longer necessary to tune interesting properties such as the QVHE. Despite that the presented results are demonstrated for lumped masses with massless string elements; the concept remains general and can be further extended to more complex geometries incorporating continuous elastic structures. Finally, this new paradigm may also be augmented with existing paradigms for initiating QVHE, including placement of unequal masses/resonators on the hexagonal lattice corners [20,21] and deliberate adjustments of structural geometry [22,35].

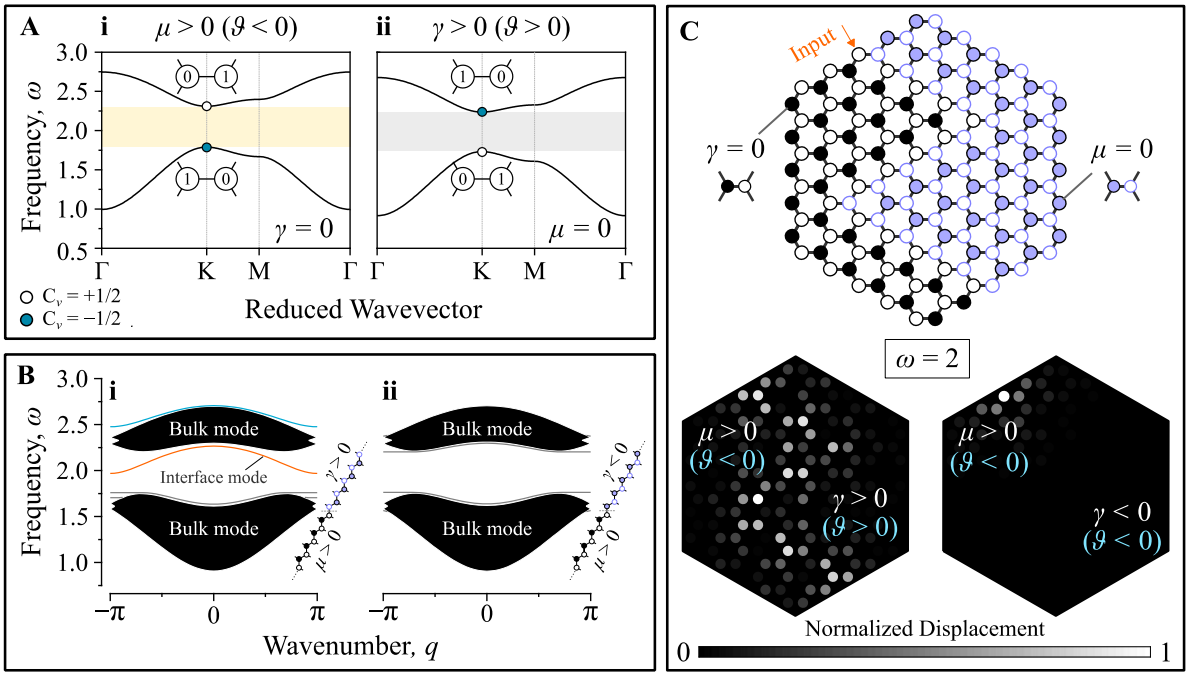

Fig. 7. (A) Dispersion diagrams for two cases of unit cells: (i) no stiffness contrast ($\gamma = 0$) and a positive mass contrast $\mu > 0$ (i.e. $\vartheta < 0$) and (ii) no mass contrast ($\mu = 0$) and a positive stiffness contrast $\gamma > 0$ (i.e. $\vartheta > 0$). The insets highlight the mode shapes at the edges of the bandgap, where band inversion between the two cases is observed. (B) Interface analysis of a supercell with different modulation types. Two cases for the signs of μ and γ are considered here: (i) both positive and (ii) positive and negative, where the interface mode arises only in the case of matching signs. (C) Illustrative schematic of a honeycomb structure with an in-homogenous modulation and the corresponding numerical analysis for an excitation frequency of $\omega = 2$ at one end of a Z-type interface. A working interface is observed only when both μ and γ being positive. A black background is added for better visualization of the displacement contour.

Declaration of competing interest

The authors declare that they have no known competing financial interests or personal relationships that could have appeared to influence the work reported in this paper.

Acknowledgment

We acknowledge the funding support from the United States Air Force Office of Scientific Research (FA9550-18-1-0192; Program manager: Dr. Ming-Jen Pan).

Appendix A. Supplementary data

Supplementary material related to this article can be found online at https://doi.org/10.1016/j.eml.2020.100758.

References

[1] M.I. Hussein, M.J. Leamy, M. Ruzzene, Dynamics of phononic materials and structures: Historical origins, recent progress, and future outlook, Appl. Mech. Rev. 66 (4) (2014).
[2] X.L. Yu, J. Zhou, H.Y. Liang, Z.Y. Jiang, L.L. Wu, Mechanical metamaterials associated with stiffness, rigidity and compressibility: A brief review, Prog. Mater. Sci. 94 (2018) 114–173.
[3] A.S. Phani, M.I. Hussein, Dynamics of Lattice Materials, Wiley Online Library, 2017.
[4] A. Banerjee, R. Das, E.P. Calius, Waves in structured mediums or metamaterials: A review, Arch. Comput. Methods Eng. 26 (4) (2019) 1029–1058.
[5] K.H. Yu, N.X. Fang, G.L. Huang, Q.M. Wang, Magnetoactive acoustic metamaterials, Adv. Mater. 30 (21) (2018).
[6] G. Trainiti, J.J. Rimoli, M. Ruzzene, Wave propagation in undulated structural lattices, Int. J. Solids Struct. 97–98 (2016) 431–444.
[7] M. Ruzzene, F. Scarpa, F. Soranna, Wave beaming effects in two-dimensional cellular structures, Smart Mater. Struct. 12 (3) (2003) 363–372.
[8] D. Tallarico, N.V. Movchan, A.B. Movchan, D.J. Colquitt, Tilted resonators in a triangular elastic lattice: Chirality, Bloch waves and negative refraction, J. Mech. Phys. Solids 103 (2017) 236–256.
[9] H. Nassar, Y.Y. Chen, G.L. Huang, A degenerate polar lattice for cloaking in full two-dimensional elastodynamics and statics, Proc. R. Soc. A-Math. Phys. Eng. Sci. 474 (2219) (2018).
[10] P. Celli, S. Gonella, Tunable directivity in metamaterials with reconfigurable cell symmetry, Appl. Phys. Lett. 106 (9) (2015).
[11] F. Casadei, J.J. Rimoli, Anisotropy-induced broadband stress wave steering in periodic lattices, Int. J. Solids Struct. 50 (9) (2013) 1402–1414.
[12] S. Tol, F.L. Degertekin, A. Erturk, Phononic crystal luneburg lens for omnidirectional elastic wave focusing and energy harvesting, Appl. Phys. Lett. 111 (1) (2017).
[13] K.H. Matlack, M. Serra-Garcia, A. Palermo, S.D. Huber, C. Daraio, Designing perturbative metamaterials from discrete models, Nature Mater. 17 (4) (2018) 323–+.
[14] Y.F. Wang, B. Yousefzadeh, H. Chen, H. Nassar, G.L. Huang, C. Daraio, Observation of nonreciprocal wave propagation in a dynamic phononic lattice, Phys. Rev. Lett. 121 (19) (2018).
[15] B.M. Goldsberry, S.P. Wallen, M.R. Haberman, Non-reciprocal wave propagation in mechanically-modulated continuous elastic metamaterials, J. Acoust. Soc. Am. 146 (1) (2019) 782–788.
[16] X.J. Zhang, M. Xiao, Y. Cheng, M.H. Lu, J. Christensen, Topological sound, Commun. Phys. 1 (2018).
[17] S.D. Huber, Topological mechanics, Nat. Phys. 12 (7) (2016) 621–623.
[18] G. Ma, M. Xiao, C.T. Chan, Topological phases in acoustic and mechanical systems, Nat. Rev. Phys. 1 (4) (2019) 281–294.
[19] H. Chen, H. Nassar, G.L. Huang, A study of topological effects in 1D and 2D mechanical lattices, J. Mech. Phys. Solids 117 (2018) 22–36.
[20] J. Vila, R.K. Pal, M. Ruzzene, Observation of topological valley modes in an elastic hexagonal lattice, Phys. Rev. B 96 (13) (2017).
[21] R.K. Pal, M. Ruzzene, Edge waves in plates with resonators: an elastic analogue of the quantum valley Hall effect, New J. Phys. 19 (2017).
[22] T.W. Liu, F. Semperlotti, Tunable acoustic valley-hall edge states in reconfigurable phononic elastic waveguides, Phys. Rev. A 9 (1) (2018).
[23] M. Miniaci, R.K. Pal, R. Manna, M. Ruzzene, Valley-based splitting of topologically protected helical waves in elastic plates, Phys. Rev. B 100 (2) (2019).
[24] A. Darabi, M.J. Leamy, Reconfigurable topological insulator for elastic waves, J. Acoust. Soc. Am. 146 (1) (2019) 773–781.
[25] Z. Tian, C. Shen, J. Li, E. Reit, H. Bachman, J.E.S. Socolar, S.A. Cummer, T. Jun Huang, Dispersion tuning and route reconfiguration of acoustic waves in valley topological phononic crystals, Nature Commun. 11 (1) (2020) 762.

[26] R. Susstrunk, S.D. Huber, Observation of phononic helical edge states in a mechanical topological insulator, Science 349 (6243) (2015) 47–50.
[27] R.K. Pal, M. Schaeffer, M. Ruzzene, Helical edge states and topological phase transitions in phononic systems using bi-layered lattices, J. Appl. Phys. 119 (8) (2016).
[28] H. Chen, L.Y. Yao, H. Nassar, G.L. Huang, Mechanical quantum hall effect in time-modulated elastic materials, Phys. Rev. A 11 (4) (2019).
[29] M.I.N. Rosa, R.K. Pal, J.R.F. Arruda, M. Ruzzene, Edge states and topological pumping in spatially modulated elastic lattices, Phys. Rev. Lett. 123 (3) (2019).
[30] R.K. Pal, M.I.N. Rosa, M. Ruzzene, Topological bands and localized vibration modes in quasiperiodic beams, New J. Phys. 21 (2019).
[31] P. Wang, L. Lu, K. Bertoldi, Topological phononic crystals with one-way elastic edge waves, Phys. Rev. Lett. 115 (10) (2015).
[32] L.M. Nash, D. Kleckner, A. Read, V. Vitelli, A.M. Turner, W.T.M. Irvine, Topological mechanics of gyroscopic metamaterials, Proc. Natl. Acad. Sci. USA 112 (47) (2015) 14495–14500.
[33] M. Garau, G. Carta, M.J. Nieves, I.S. Jones, N.V. Movchan, A.B. Movchan, Interfacial waveforms in chiral lattices with gyroscopic spinners, Proc. R. Soc. A-Math. Phys. Eng. Sci. 474 (2215) (2018).
[34] L. Liu, M.I. Hussein, Wave motion in periodic flexural beams and characterization of the transition between bragg scattering and local resonance, J. Appl. Mech.-Trans. Asme 79 (1) (2012).
[35] Z.L. Du, H. Chen, G.L. Huang, Optimal quantum valley Hall insulators by rationally engineering Berry curvature and band structure, J. Mech. Phys. Solids 135 (2020).
[36] S. Gonella, M. Ruzzene, Analysis of in-plane wave propagation in hexagonal and re-entrant lattices, J. Sound Vib. 312 (1–2) (2008) 125–139.
[37] H. Chen, H. Nassar, A.N. Norris, G.K. Hu, G.L. Huang, Elastic quantum spin Hall effect in kagome lattices, Phys. Rev. B 98 (9) (2018).
[38] Y. Chen, X.N. Liu, G.K. Hu, Topological phase transition in mechanical honeycomb lattice, J. Mech. Phys. Solids 122 (2019) 54–68.
[39] H.F. Zhu, T.W. Liu, F. Semperlotti, Design and experimental observation of valley-Hall edge states in diatomic-graphene-like elastic waveguides, Phys. Rev. B 97 (17) (2018).
[40] E. Riva, D.E. Quadrelli, G. Cazzulani, F. Braghin, Tunable in-plane topologically protected edge waves in continuum Kagome lattices, J. Appl. Phys. 124 (16) (2018).
[41] M.A. Nouh, O.J. Aldraihem, A. Baz, Periodic metamaterial plates with smart tunable local resonators, J. Intell. Mater. Syst. Struct. 27 (13) (2016) 1829–1845.
[42] G. Trainiti, Y.W. Xia, J. Marconi, G. Cazzulani, A. Erturk, M. Ruzzene, Time-periodic stiffness modulation in elastic metamaterials for selective wave filtering: Theory and experiment, Phys. Rev. Lett. 122 (12) (2019).
[43] C. Yang, M. Boorugu, A. Dopp, J. Ren, R. Martin, D. Han, W. Choi, H. Lee, 4d printing reconfigurable, deployable and mechanically tunable metamaterials, Mater. Horiz. 6 (6) (2019) 1244–1250.

Supplementary Information:

Elastically-Supported Lattices for Tunable Mechanical Topological Insulators

Hasan Al Ba'ba'a, Kunhao Yu, and Qiming Wang[1]

Sonny Astani Department of Civil and Environmental Engineering, University of Southern California, Los Angeles, CA 90089, USA

[1] Corresponding Author; Email: qimingw@usc.edu

List of Supplementary Notes:

List of Supplementary Figures:

Note 1 Analytical Derivation of Berry Curvature

In this note, we provide a detailed derivation for the exact analytical form of Berry Curvature, which can be derived from the following expression:

$$\mathcal{F}_{\pm}(\boldsymbol{q}) = \frac{\mathbf{i}}{4|\lambda|^2}\left[\left[\mathbf{x}_{\mp}^{\mathbf{T}}\frac{\partial \boldsymbol{\mathcal{H}}}{\partial q_x}\mathbf{x}_{\pm}\mathbf{x}_{\pm}^{\mathbf{T}}\frac{\partial \boldsymbol{\mathcal{H}}}{\partial q_y}\mathbf{x}_{\mp}\right] - \boldsymbol{c}.\boldsymbol{c}.\right] \tag{1}$$

We first express the eigenvector of the unit-cell's Hamiltonian as:

$$\mathbf{x}_{\pm} = \frac{1}{\sqrt{2}}\begin{Bmatrix} e^{\frac{-\mathrm{i}\phi}{2}}x_{\pm} \\ \mp e^{\frac{+\mathrm{i}\phi}{2}}x_{\mp} \end{Bmatrix} \tag{2}$$

where $\phi = \arg(\varepsilon)$ and

$$x_{\pm} = \sqrt{\left(1 \pm \frac{\vartheta}{|\lambda|}\right)} \tag{3}$$

Next, we evaluate the derivatives of the Hamiltonian (Equation (18) in the main text) which have the following explicit forms:

$$\frac{\partial \boldsymbol{\mathcal{H}}}{\partial q_x} = -\mathrm{i}\sqrt{3}\cos\left(\frac{q_y}{2}\right)\begin{bmatrix} 0 & -z_x^* \\ z_x & 0 \end{bmatrix} \tag{4}$$

$$\frac{\partial \boldsymbol{\mathcal{H}}}{\partial q_y} = -\begin{bmatrix} 0 & \dfrac{\partial \varepsilon^*}{\partial q_y} \\ \dfrac{\partial \varepsilon}{\partial q_y} & 0 \end{bmatrix} = \sin\left(\frac{q_y}{2}\right)\begin{bmatrix} 0 & z_x^* \\ z_x & 0 \end{bmatrix} \tag{5}$$

where $z_x = e^{\mathrm{i}\frac{\sqrt{3}}{2}q_x}$ is introduced for mathematical convenience. Substituting back into the term between brackets in Equation (1) yields the following equation:

$$\begin{aligned} &\mathbf{x}_{\mp}^{\mathbf{T}}\frac{\partial \boldsymbol{\mathcal{H}}}{\partial q_x}\mathbf{x}_{\pm}\mathbf{x}_{\pm}^{\mathbf{T}}\frac{\partial \boldsymbol{\mathcal{H}}}{\partial q_y}\mathbf{x}_{\mp} \\ &\quad = \frac{\mathrm{i}\sqrt{3}}{4}\cos\left(\frac{q_y}{2}\right)\sin\left(\frac{q_y}{2}\right)\left[z_x e^{-\mathrm{i}\phi}x_{\mp}^2 - z_x^* e^{+\mathrm{i}\phi}x_{\pm}^2\right]\left[z_x e^{-\mathrm{i}\phi}x_{\pm}^2 \right. \\ &\quad \left. + z_x^* e^{\mathrm{i}\phi}x_{\mp}^2\right] \end{aligned} \tag{6}$$

which, after few mathematical manipulations, reduces to:

$$\mathbf{x}_{\mp}^{\mathbf{T}} \frac{\partial \boldsymbol{\mathcal{H}}}{\partial q_x} \mathbf{x}_{\pm} \mathbf{x}_{\pm}^{\mathbf{T}} \frac{\partial \boldsymbol{\mathcal{H}}}{\partial q_y} \mathbf{x}_{\mp} = \frac{\mathrm{i}\sqrt{3}}{8} \sin(q_y) \left[x_{\mp}^2 x_{\pm}^2 \left[z_x^2 e^{-2\mathrm{i}\phi} - z_x^{*2} e^{2\mathrm{i}\phi} \right] + x_{\mp}^4 - x_{\pm}^4 \right] \tag{7}$$

Making use of $\varepsilon = |\varepsilon| e^{\mathrm{i}\phi}$ and the following derived expressions: $\left(x_{\mp}^2 + x_{\pm}^2\right) = 2$, $\left(x_{\pm}^2 - x_{\mp}^2\right) = \pm 2 \frac{\vartheta}{|\lambda|}$ and $x_{\mp}^2 x_{\pm}^2 = \frac{|\varepsilon|^2}{|\lambda|^2}$, the above expression boils down to:

$$\mathbf{x}_{\mp}^{\mathbf{T}} \frac{\partial \boldsymbol{\mathcal{H}}}{\partial q_x} \mathbf{x}_{\pm} \mathbf{x}_{\pm}^{\mathbf{T}} \frac{\partial \boldsymbol{\mathcal{H}}}{\partial q_y} \mathbf{x}_{\mp} = \frac{\mathrm{i}\sqrt{3}}{8} \sin(q_y) \left[\frac{1}{|\lambda|^2} [z_x^2 \varepsilon^{*2} - z_x^{*2} \varepsilon^2] \pm 4 \frac{\vartheta}{|\lambda|} \right] \tag{8}$$

Computing the complex conjugate of Equation (8) and taking the difference of the conjugate pair, we obtain

$$\mathbf{x}_{\mp}^{\mathbf{T}} \frac{\partial \boldsymbol{\mathcal{H}}}{\partial q_x} \mathbf{x}_{\pm} \mathbf{x}_{\pm}^{\mathbf{T}} \frac{\partial \boldsymbol{\mathcal{H}}}{\partial q_y} \mathbf{x}_{\mp} - \left(\mathbf{x}_{\mp}^{\mathbf{T}} \frac{\partial \boldsymbol{\mathcal{H}}}{\partial q_x} \mathbf{x}_{\pm} \mathbf{x}_{\pm}^{\mathbf{T}} \frac{\partial \boldsymbol{\mathcal{H}}}{\partial q_y} \mathbf{x}_{\mp} \right)^* = \mathrm{i}\sqrt{3} \sin(q_y) \left[\pm \frac{\vartheta}{|\lambda|} \right] \tag{9}$$

Which ultimately leads to the final form of the Berry curvature (i.e. Equation (37) in the main text):

$$\mathcal{F}_{\pm}(\boldsymbol{q}) = \frac{\mp\sqrt{3}\vartheta}{4|\lambda|^3} \sin(q_y) = \frac{\mp\sqrt{3}\vartheta \sin(q_y)}{4\sqrt{(\vartheta^2 + |\varepsilon|^2)^3}} \tag{10}$$

Note 2 Mathematical Formulation for a Single Strip of Hexagonal Lattice

For the strip analysis, we start by considering a one-dimensional chain of the hexagonal lattice, where the order of periodicity is flipped midway. We shall next apply a Bloch wave solution on the orthogonal direction of the chain's periodicity to emulate an interface extended in the second spatial direction. As such, the dynamics of a strip with a size of $2n$ is described by:

$$\mathbf{M_I} \ddot{\mathbf{z}}(t) + \mathbf{K_I}(q) \mathbf{z}(t) = \mathbf{0} \tag{11}$$

where

$$\mathbf{M_I} = m \begin{bmatrix} \mathbf{I}_n + \mu \mathbf{V} & \\ & \mathbf{I}_n - \mu \mathbf{V} \end{bmatrix} \tag{12}$$

$$\mathbf{K_I}(q) = k\kappa \begin{bmatrix} \mathbf{I}_n + \gamma \mathbf{V} & \mathbf{0} \\ \mathbf{0} & \mathbf{I}_n - \gamma \mathbf{V} \end{bmatrix} + k \boldsymbol{\Psi}_{\mathbf{I}}(q) \tag{13}$$

$$\boldsymbol{\Psi}_{\mathbf{I}}(q) = \begin{bmatrix} 3 & -(1+\mathrm{e}^{-\mathbf{i}q}) & & & & & & & \\ -(1+\mathrm{e}^{\mathbf{i}q}) & 3 & -1 & & & & & & \\ & -1 & 3 & -(1+\mathrm{e}^{-\mathbf{i}q}) & & & & & \\ & & -(1+\mathrm{e}^{\mathbf{i}q}) & \ddots & \ddots & & & & \\ & & & \ddots & \ddots & \ddots & & & \\ & & & & \ddots & \ddots & -1 & & \\ & & & & & -1 & 3 & -(1+\mathrm{e}^{-\mathbf{i}q}) & \\ & & & & & & -(1+\mathrm{e}^{\mathbf{i}q}) & 3 & \end{bmatrix} \quad (14)$$

The unit matrix $\mathbf{I}_n$ and diagonal matrix $\mathbf{V}$ are of size $n \times n$, where the latter has the following definition:

$$V_i = \begin{cases} +1, & \mathbf{mod}(i,2) = 1 \\ -1, & \mathbf{mod}(i,2) = 0 \end{cases} \quad (15)$$

Solving for the eigenvalues over a complete cycle of the wavenumber $q \in [-\pi, \pi]$ produces a set of eigenpairs, which can be categorized (based on relevant dispersion analysis) as bulk or interface modes depending on their frequency range.

Note 3 Equations of Motion of Honeycomb Structures

For the numerical simulation of waveguides, we construct a finite lattice with a honeycomb structural shape (Figure S1**A**) to validate the predictions obtained from the unit-cell's dispersion diagrams and demonstrate the emergence of waveguides. The honeycomb structure consists of a total number of masses n_t and the masses on the sides are fixed along the boundaries via springs k. Due to the honeycomb structural shape, the total number of masses can be represented as a function of the number of masses on the sides, denoted here as n_s. Starting from one of the sides and propagating towards its opposite peer, the total number of the masses is expressed via a simple formula:

$$n_t = 6n_s^2 \quad (16)$$

Which is graphically illustrated via several values of n_s in Figure S1**B**. Generally, the equations of motion of a honeycomb lattice can be presented in a compact matrix notation as follows:

$$\mathbf{M_g}\ddot{\mathbf{z}}(t) + \mathbf{K_g}\mathbf{z}(t) = \mathbf{f}(t) \quad (17)$$

Where

$$\mathbf{z}(t) = \{z_1(t)\ z_2(t) \cdots z_{n_t}(t)\}^T \tag{18}$$

is the displacement vector (the degrees of freedom ordering is shown in Figure S1**A**) and $\mathbf{f}(t)$ is the forcing vector. The global stiffness matrix $\mathbf{K_g}$ constitutes of two parts: the main structure and elastic foundation stiffness matrices, $\mathbf{K}_s$ and $\mathbf{K}_f$, respectively, and the addition of which provides the global stiffness matrix, i.e. $\mathbf{K_g} = \mathbf{K}_f + \mathbf{K}_s$. The elastic foundation's stiffness matrix is a diagonal matrix and can be expressed as:

$$\mathbf{K}_f = \mathbf{diag}[k_1, k_2, \dots, k_{n_t}] \tag{19}$$

where the spring constants k_1 through k_{n_t} depend on the design of the elastic waveguide. The stiffness matrix of the main structure, on the other hand, is given by a block tridiagonal matrix:

$$\mathbf{K}_s = k\begin{bmatrix}
\boldsymbol{\Psi}_1 & \mathbf{S}_1 & & & & & & & & \\
\mathbf{S}_1^{\mathbf{T}} & \boldsymbol{\Psi}_2 & \mathbf{S}_2 & & & & & & & \\
 & \mathbf{S}_2^{\mathbf{T}} & \ddots & \ddots & & & & & & \\
 & & \ddots & \ddots & \mathbf{S}_{n_s-1} & & & & & \\
 & & & \mathbf{S}_{n_s-1}^{\mathbf{T}} & \boldsymbol{\Psi}_{n_s} & \hat{\mathbf{S}}_{n_s} & & & & \\
 & & & & \hat{\mathbf{S}}_{n_s} & \boldsymbol{\Psi}_{n_s} & \mathbf{S}_{n_s-1}^{\mathbf{T}} & & & \\
 & & & & & \mathbf{S}_{n_s-1} & \boldsymbol{\Psi}_{n_s-1} & \mathbf{S}_{n_s-2}^{\mathbf{T}} & & \\
 & & & & & & \mathbf{S}_{n_s-2} & \ddots & \ddots & \\
 & & & & & & & \ddots & \ddots & \mathbf{S}_1^{\mathbf{T}} \\
 & & & & & & & & \mathbf{S}_1 & \boldsymbol{\Psi}_1
\end{bmatrix} \tag{20}$$

Where $\boldsymbol{\Psi}_r$ is an $N_r \times N_r$ tridiagonal matrix, where $N_r = 2(n_s + r) - 1$, $r = 1,2, \dots, n_s$ and its entries Ψ_{ij} are defined as:

$$\Psi_{ij} = \begin{cases} 3, & i = j \\ -1, & |i-j| = 1 \\ 0, & |i-j| \neq 1,0 \end{cases} \tag{21}$$

The off-diagonal submatrix $\mathbf{S}_r$ in Equation (20) is of size $N_r \times N_{r+1}$ and given by:

$$\mathbf{S}_r = [\mathbf{0}\ \hat{\mathbf{S}}_r\ \mathbf{0}] \tag{22}$$

where $\mathbf{0}$ is a single column of zeros and $\hat{\mathbf{S}}$ is a square diagonal matrix of size $N_r \times N_r$ with the following entries:

$$\hat{S}_i = \begin{cases} -1, & \mathbf{mod}(i,2) = 1 \\ 0, & \mathbf{mod}(i,2) = 0 \end{cases} \tag{23}$$

such that $\mathbf{mod}(\cdot)$ is the modulo function. Finally, the global mass matrix $\mathbf{M_g}$ is a diagonal matrix of the form:

$$\mathbf{M_g} = \mathbf{diag}[m_1, m_2, \dots, m_{n_t}] \tag{24}$$

and the mass values m_1 through m_{n_t} depend on the structure's waveguide design in analogy to the elastic foundation stiffness matrix in Equation (19). If the system is perfectly periodic (i.e. a regular honeycomb structure with no waveguide), then the mass matrix follows a periodic pattern:

$$\mathbf{M_g} = m\mathbf{I}_{n_t} + m\begin{bmatrix} \mu\mathbf{V}_1 & & & & & \\ & \ddots & & & & \\ & & \mu\mathbf{V}_{n_s} & & & \\ & & & -\mu\mathbf{V}_{n_s} & & \\ & & & & \ddots & \\ & & & & & -\mu\mathbf{V}_1 \end{bmatrix} \tag{25}$$

where $\mathbf{I}_{n_t}$ is a unit matrix of size $n_t \times n_t$ and $\mathbf{V}_r$ is an $N_r \times N_r$ diagonal matrix and its definition follows Equation (15). Similarly, the stiffness matrix for the elastic foundation can be expressed using the periodic form in Equations (25) and (15):

$$\mathbf{K}_f = k\kappa\mathbf{I}_{n_t} + k\kappa\begin{bmatrix} \gamma\mathbf{V}_1 & & & & & \\ & \ddots & & & & \\ & & \gamma\mathbf{V}_{n_s} & & & \\ & & & -\gamma\mathbf{V}_{n_s} & & \\ & & & & \ddots & \\ & & & & & -\gamma\mathbf{V}_1 \end{bmatrix} \tag{26}$$

Note 4 Effect of Design Parameters on Dispersion and Topological Aspects

Tuning parameter ϑ and central bandgap frequency Ω_s (Given by Equations (19) and (20) in the main text) symbolize the main two variables for dictating the wave dispersion characteristics of the hexagonal lattice under consideration. These two variables are functions of the mass and stiffness contrast: μ and γ, respectively, as well as the stiffness ratio κ. Starting with the tuning parameter ϑ, for a given stiffness ratio κ, it can assume negative or positive values depending on the signs of μ and γ, which can be summarized in **Table 1**. The central bandgap frequency is also

dependent on the signs of μ and γ, specifically on their multiplication. **Figure S2 A(B)** depicts several combinations of the μ (γ) and their effect on the tuning parameter and central frequency for a swept range of γ (μ). It is observed that as the value of μ (γ) increases, the corresponding value of ϑ monotonically decreases (increases), until it changes its sign. The central bandgap frequency, on the other hand, has a symmetrical profile for a change in the sign of μ and γ about its zero value $\mu = 0$ ($\gamma = 0$) in both cases.

Table 1. Combinations of the mass and stiffness contrasts and their influence on the tuning parameter ϑ.

	γ	μ	***Comments***
1	$+$	$+$	$\vartheta > 0$ when $\gamma > \frac{3+\kappa}{\kappa}\mu$ and vice versa
2	$+$	$-$	$\vartheta > 0$ for all values of μ and γ
3	$-$	$+$	$\vartheta < 0$ for all values of μ and γ
4	$-$	$-$	$\vartheta > 0$ when $\gamma < \frac{3+\kappa}{\kappa}\mu$ and vice versa

The system parameters have a further impact on the distribution of the natural frequencies on a honeycomb structure, specifically the modes appear inside the bandgaps and stop-band. If we consider the interface I as a case in point, a binary search for natural frequencies, depicted in Figure **S3A(i)** and **A(iii)**, in the zero-frequency bandgap ($\Omega < \Omega_z$), and the stop-band ($\Omega > \Omega_c$), surprisingly reveals that the emergence of natural frequencies within the aforementioned regions does not necessarily follow the topological transition line ($\gamma = 4\mu$ for this case), and heavily rely on the inertial and elastic parameters (μ and γ, respectively). Nonetheless, an interface mode within the main bandgap in the range $\Omega_l < \Omega < \Omega_u$ is unequivocally certain for all non-zero values of ϑ (Figure **S3A(ii)**).

Note 5 Additional Analysis of In-Homogenous Waveguide Design

Figure S4 and **Figure S5** represent additional analysis of the strip analysis of in-homogenous interface and different shapes of waveguiding.

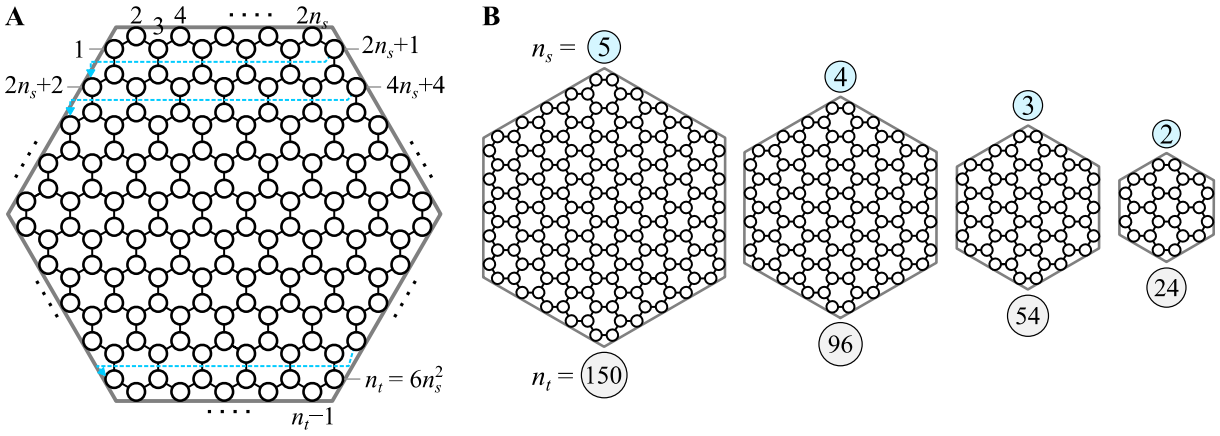

Figure S1. Finite honeycomb structure illustrative schematics: (**A**) degrees of freedom numbering (rotated 30° clockwise for better visualization) and (**B**) total number of degrees of freedom n_t calculations based on the number of mass on the honeycomb sides n_s.

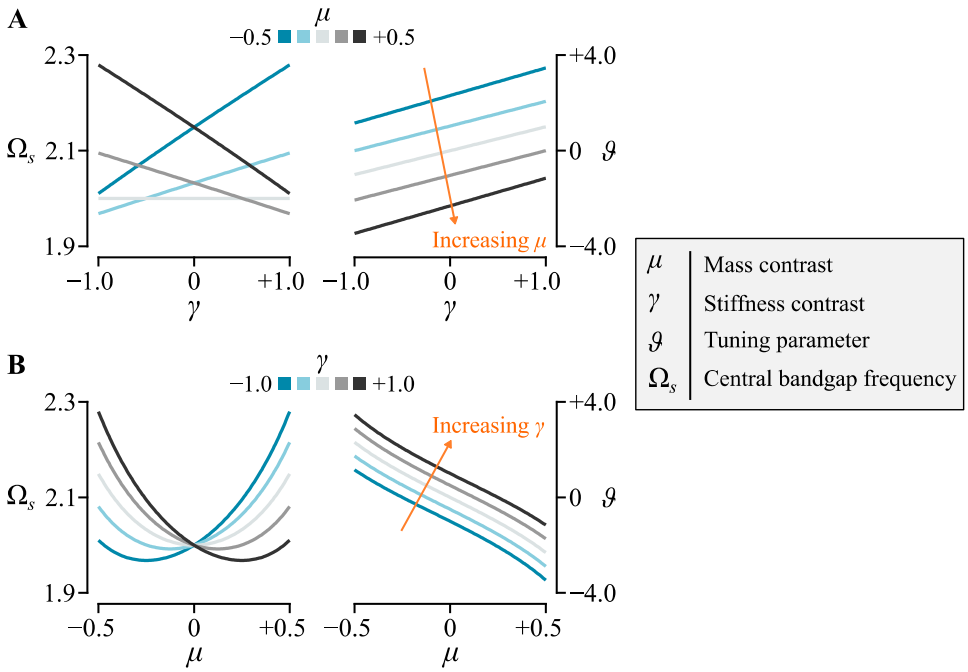

Figure S2 (**A,B**) Effect of changing the mass (stiffness) contrast over a swept range of stiffness (mass) contrast on the tuning parameter and bandgap central frequency.

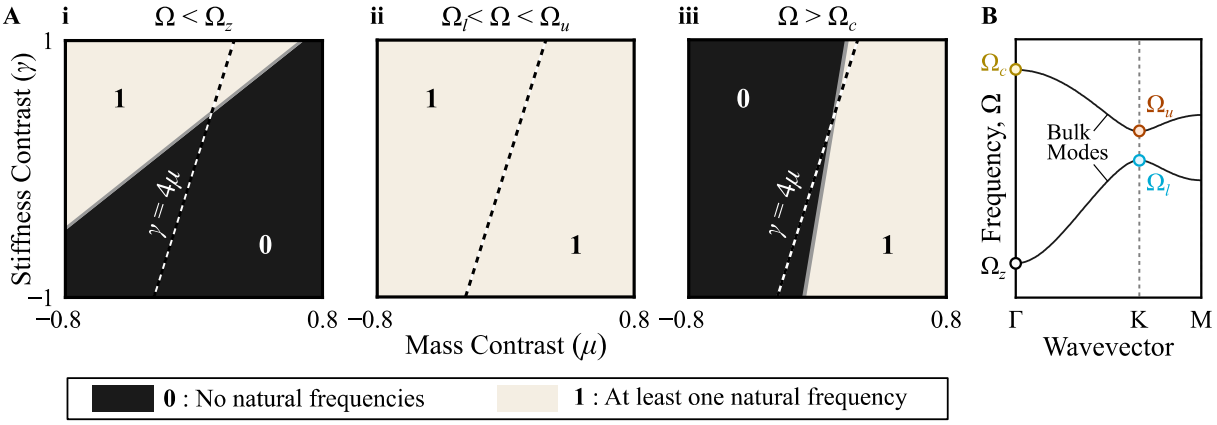

Figure S3. (**A**) Binary search of natural frequencies as a function of the mass and stiffness contrasts (**i**) inside the zero-frequency bandgap (i.e. $\Omega < \Omega_z$), (**ii**) bulk bandgap (i.e. $\Omega_- < \Omega < \Omega_+$), (**iii**) and above the cutoff frequency (i.e. $\Omega > \Omega_c$). (**B**) A typical dispersion diagram for hexagonal lattice shown as a key to interpret subfigure **A** and illustrates the location of frequencies related to the natural frequencies search.

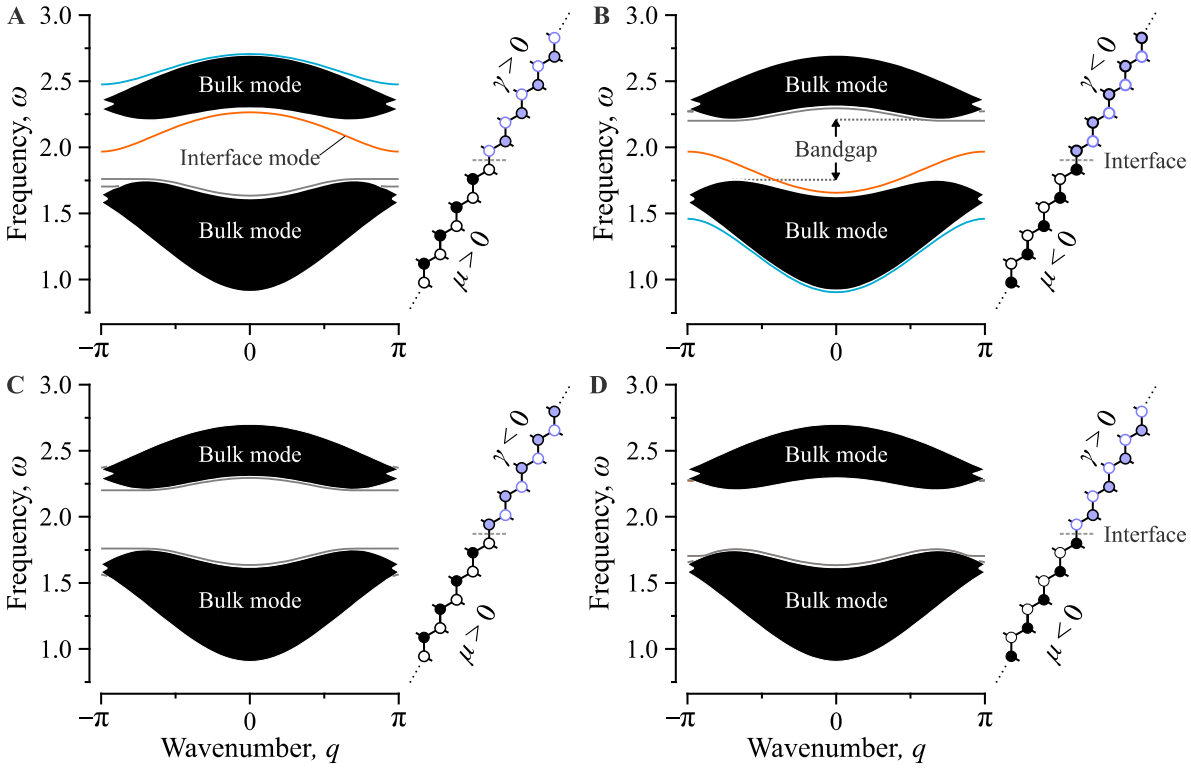

Figure S4. Eigenfrequency analysis of a supercell comprised of a finite number of masses with different modulation types, namely mass and stiffness modulations, about a defined interface. Four cases for the signs of μ and γ are considered here: (**A**) both positive, (**B**) both negative, (**C**) positive negative, and (**D**) negative positive. Edge modes within the bandgap range arise only with cases of matching signs.

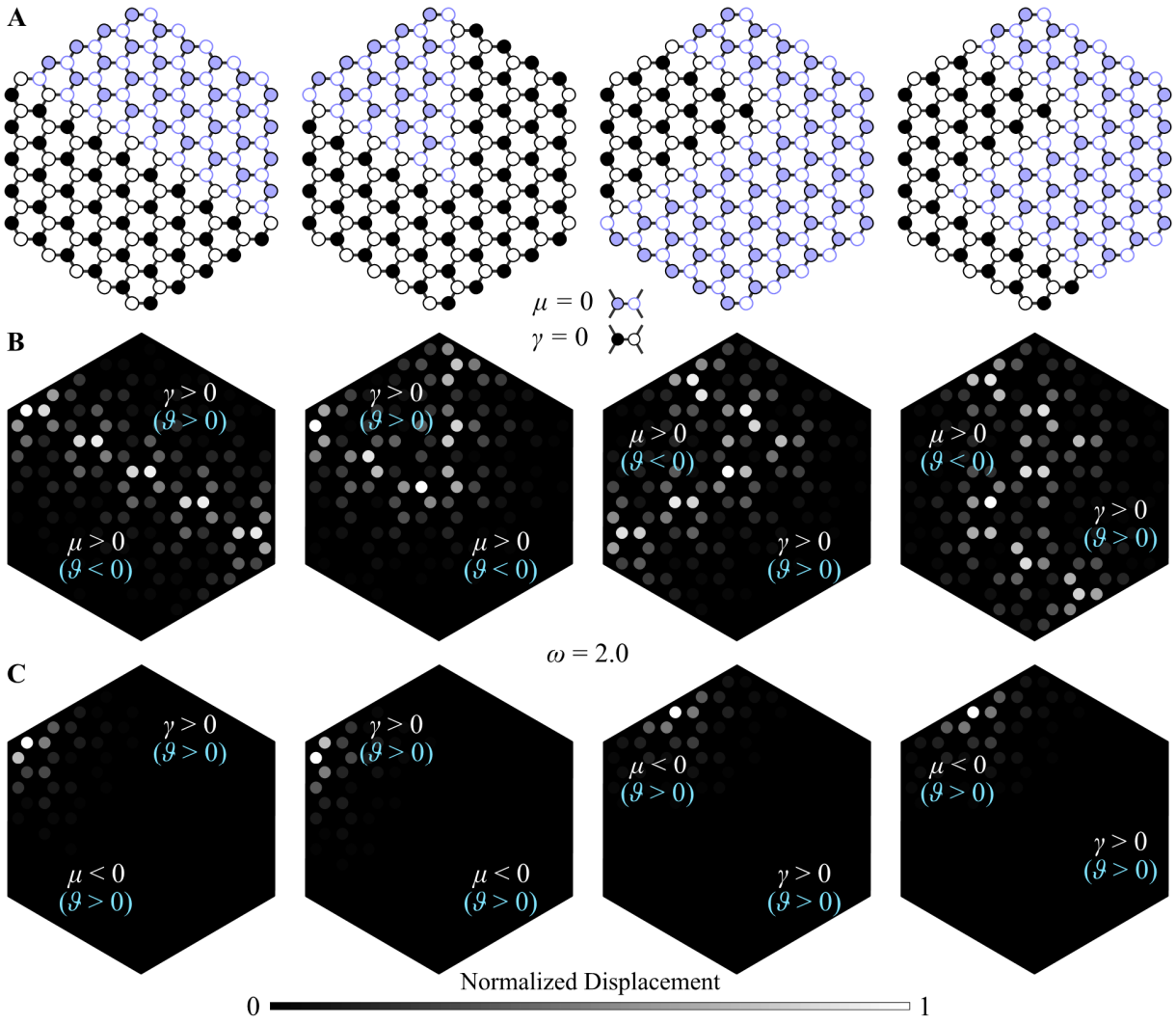

Figure S5. (A) Illustrative schematics of in-homogenous modulation in a honeycomb structure. Numerical analysis of the structures in (A) for an excitation frequency of $\omega = 2$ at one end of the different interfaces with (B) mass contrast and stiffness contrast being positive, resulting in a working interface. The mass and stiffness modulations in subfigure (C) possess different signs (i.e. $\mu\gamma < 0$), rendering the interface trivial. A black background is added in subfigures B and C for better visualization of the results.